Acta Mech 195, 227–247 (2008)
DOI 10.1007/s00707-007-0571-4
Printed in The Netherlands

Acta Mechanica

Dedicated to Professor Franz Ziegler on the occasion of his 70th birthday

Acoustic modeling of light and non-cohesive poro-granular materials with a fluid/fluid model

J.-D. Chazot[1], J.-L. Guyader[2]

[1] Laboratoire Roberval, Centre de Recherches de Royallieu, Université de Technologie de Compiègne, Compiègne Cedex, France
[2] INSA de Lyon, Laboratoire Vibrations Acoustique, Antoine de Saint Exupery, Villeurbanne, France

Received 8 October 2007; Accepted 4 December 2007; Published online 15 January 2008

Summary. Poro-granular materials are studied, and a model adapted to characterize their acoustic behaviour is presented. Biot's theory is used to obtain this model but a great simplification is brought to classical formulation. Indeed, a solid phase being made of a non-cohesive poro-granular material, a specific continuum constitutive model is used to characterize its behaviour. The macroscopic coefficient of friction that takes into account friction and collision phenomena is then neglected under specific conditions. This strong assumption does not apply for all kinds of granular materials and for any solicitations: its validity is discussed for particular materials. The solid/fluid model of Biot's theory is then transformed to an equivalent fluid/fluid model. The complexity of the classical formulation is significantly reduced since only two degrees of freedom are used: the solid and fluid pressures. A 1D case is then treated to present the simplicity of the formulation, and applied to a poro-granular material made of expanded polystyrene beads. Intrinsic parameters of this material are adjusted thanks to surface impedances measured with a stationary waves tube. Finally, a study on thermal and viscous dissipations is realized and associated with a study on pressure and velocity distribution in the sample.

1 Introduction

Acoustic properties of granular materials are investigated in this paper. Like porous materials, it is important to take into account both solid and fluid phases, and thermal and viscous interactions between them. To this aim, Biot's theory can be used. However, the solid phase being made of a non-cohesive poro-granular material, it cannot be considered as an isotropic elastic continuum. Moreover, the granular solid phase can exhibit different behaviours depending on the excitation conditions: a quasi–static behaviour, a rapid granular flow behaviour, or an intermediate behaviour. A specific continuum constitutive model adapted to the granular material and its excitation conditions is therefore necessary to model this granular solid phase.

In this paper, Biot's model is adapted to light and non-cohesive poro-granular materials. After some simplifications, a fluid–fluid model is obtained with only two degrees of freedom: a fluid

Correspondence: J.-D. Chazot, Laboratoire Roberval, Centre de Recherches de Royallieu, Université de Technologie de Compiègne, BP 20529, 60205 Compiègne Cedex, France
e-mail: jean-daniel.chazot@utc.fr

pressure and a solid pressure. An efficient numerical method can then be used to characterize a granular material sample thanks to these simplifications.

An expanded polystyrene beads sample is then studied. Its surface impedance is measured with a stationary waves tube. This measurement is used to adjust the fluid–fluid model, and intrinsic parameters of this granular material sample are hence determined. A comparison with data found in literature, and with direct measurements carried out with a 3D micro-tomograph is used to confirm the validity of the results.

Finally, the adjusted model is used to study thermal and viscous dissipations inside the poro-granular sample. A study on pressures and velocities distributions is also realized to understand these dissipations phenomena.

2 State of the art

Porous materials are commonly employed for sound insulation in several domains such as aeronautics and automotive. It is thus of the utmost important to be able to characterize their behaviour in a real context. During the past decades, porous materials have been widely studied and models have been established to predict their acoustical and mechanical behaviours [1], [2]. Two kinds of models can be found in literature: models based on a fluid equivalent description [3], [4] and models based on Biot's theory. Fluid equivalent models take into account viscous and thermal effects using frequency dependent expressions of fluid dynamic compressibility K_{f} and fluid dynamic density ρ_{f}. These expressions can be related to the geometrical characteristics of the pores [5]–[7]. Basically, five parameters are of interest: porosity ϕ, tortuosity α_∞, viscous permeability k_0 (related to air flow resistivity by $\sigma = \eta/k_0$ with η the dynamic fluid viscosity), and viscous and thermal characteristic lengths (respectively, Λ and Λ'). Expressions given in Eq. (1), where Pr is the Prandtl number, and detailed in [8] can for example be used to describe the microgeometry structure with five parameters:

$$\begin{aligned}
\rho_{\mathrm{f}}(\omega) &= \rho_0 \alpha_\infty \left(1 + \frac{\eta\phi}{i\rho_0\alpha_\infty k_0 \omega}\sqrt{1 + 4\frac{k_0^2\alpha_\infty^2 i\omega\rho_0}{\Lambda^2\phi^2\eta}}\right), \\
K_{\mathrm{f}}(\omega) &= \frac{\gamma P_0}{\gamma - (\gamma-1)\left(1 + \frac{8\eta}{i\Lambda'^2 Pr\rho_0\omega}\sqrt{1 + i\rho_0\frac{Pr\Lambda'^2\omega}{16\eta}}\right)^{-1}}.
\end{aligned} \tag{1}$$

However, fluid equivalent models do not take into account solid phase elasticity that is assumed to be totally rigid. On the contrary, Biot's theory [9]–[11] based models consider not only solid phase elasticity, but also elastic and inertial coupling between solid and fluid phases.

Elastic coupling is hence taken into account in Biot's poroelasticity equations recalled in Eq. (2) and detailed in [12]. Solid and fluid stress tensors, (respectively, $\underline{\underline{\sigma}}^s$ and $\underline{\underline{\sigma}}^f$) are here related to both solid and fluid strain tensors, (respectively, $\underline{\underline{\varepsilon}}^s$ and $\underline{\underline{\varepsilon}}^f$).

$$\begin{aligned}
\underline{\underline{\sigma}}^{\mathrm{s}} &= 2N\underline{\underline{\varepsilon}}^{\mathrm{s}} + [P - 2N]tr(\underline{\underline{\varepsilon}}^{\mathrm{s}})\underline{\underline{1}} + Qtr(\underline{\underline{\varepsilon}}^{\mathrm{f}})\underline{\underline{1}}, \\
\underline{\underline{\sigma}}^{\mathrm{f}} &= Rtr(\underline{\underline{\varepsilon}}^{\mathrm{f}})\underline{\underline{1}} + Qtr(\underline{\underline{\varepsilon}}^{\mathrm{s}})\underline{\underline{1}}.
\end{aligned} \tag{2}$$

The elastic coefficients P, N, Q and R depend on the following solid and fluid properties: solid bulk modulus K_{b}, solid shear modulus N, dynamic fluid compressibility K_{f}, and porosity ϕ. Their simplified expressions are given in Eq. (3). These simplified expressions are based on the assumption that the solid phase bulk modulus is much higher than the skeleton bulk modulus and also much higher than the one of air:

$$\begin{aligned} P &= \frac{4}{3}N + K_{\mathrm{b}} + \frac{(1-\phi)^2 K_{\mathrm{f}}}{\phi}, \\ Q &= K_{\mathrm{f}}(1-\phi), \\ R &= \phi K_{\mathrm{f}}. \end{aligned} \tag{3}$$

Inertial coupling is taken into account in local equilibrium equations presented in Eq. (4) where stress tensors are related to both solid and fluid acceleration vectors (respectively, $\vec{\gamma}^{s}$ and $\vec{\gamma}^{f}$), and to local forces $\vec{f}_v$ and $\vec{f}_v$:

$$\begin{aligned} \overrightarrow{\mathrm{div}}(\underline{\underline{\sigma}}^{\mathrm{s}}) + \vec{f}_v^{\,\mathrm{s}} &= \rho_{11}\vec{\gamma}^{\mathrm{s}} + \rho_{12}\vec{\gamma}^{\mathrm{f}}, \\ \overrightarrow{\mathrm{div}}(\underline{\underline{\sigma}}^{\mathrm{f}}) + \vec{f}_v^{\,\mathrm{f}} &= \rho_{22}\vec{\gamma}^{\mathrm{f}} + \rho_{12}\vec{\gamma}^{\mathrm{s}}. \end{aligned} \tag{4}$$

An inertial coupling coefficient ρ_{12} is used here to take into account inertial effects (added mass) on solid and fluid phases. Viscous tangential effects are also included via solid and fluid equivalent densities (respectively, ρ_{11} and ρ_{22}). Expressions of the densities ρ_{11}, ρ_{12} and ρ_{22} are recalled in Eq. (5) where ρ_{s} and ρ_{f} are, respectively, the solid and fluid density, ϕ is the porosity, and α_∞ is the tortuosity,

$$\begin{aligned} \rho_{11} &= (1-\phi)\rho_{\mathrm{s}} + \phi\rho_{\mathrm{f}}(\alpha_\infty - 1), \\ \rho_{12} &= -\phi\rho_{\mathrm{f}}(\alpha_\infty - 1), \\ \rho_{22} &= \phi\rho_{\mathrm{f}}\alpha_\infty. \end{aligned} \tag{5}$$

As in fluid equivalent models, viscous and thermal effects are also taken into account in Biot's theory based models with a dynamic fluid compressibility K_{f} and a fluid density ρ_{f}. Expressions given in Eq. (1) are still valid in Biot's theory based models, and five intrinsic parameters are thus necessary. Several kinds of characterization, direct or not, can be used [13] to get these parameters. Some are based on transmitted waves measurements [14]. Others are based on a microscopic study of the material with a 3D microtomograph [15]. And finally, an inverse acoustic measurement can also be used to adjust these parameters [16]–[18].

Before the recent march of numerical methods, the Transfer Matrix Method was used to characterize a porous media with Biot's theory [8], [19]. However, this method is limited to simple structures with academic geometries. Nowadays, numerical methods, such as the finite element method, are used in all kinds of domains for complex structures. In the domain of poroelastic materials modeling [20], a displacement formulation [21] and a mixed displacement–pressure formulation [22]–[24] have been developed, for example.

However, till now, all numerical methods applied to poroelastic materials have still been limited by time computation and computation efficiency for a large size model at medium frequencies, in part due to severe meshing rules [25]. Recent works have thus been focused on alternative ways to improve these performances. An extension of complex modes for the resolution of finite-element poroelastic problems [26], and an alternative Biot's displacement formulation for porous materials [27] have been proposed to enhance the efficiency of numerical method for porous materials. Other numerical tools have also permitted to study a fully trimmed vehicle using modified Biot's theory [28]. However, numerical methods used for poroelastic materials are still facing difficulties to go at high frequencies with large models. These difficulties can be overcome by a simplification of the Biot model. A limp model can for example be used to this aim [29], but this model is limited to some specific materials. In the same way, this paper proposes a simplified model adapted to specific materials: light and non-cohesive poro-granular materials.

One of the interesting aspects of granular media is their ability to damp hollow structures. Different approaches are used to study this added damping [30]–[35]. However, viscous damping due to solid fluid interactions is not taken into account in these studies, and the dissipation mechanism is only modeled with friction and shocks between the particles.

Acoustic properties of granular materials have also been studied in the past. An empirical model has for example been proposed for loose granular media [36]. However, models dedicated to porous materials are generally employed as is for granular materials [37]. Hence fluid equivalent model and Biot's model have been applied to granular materials such as sand or glass beads. Differences between a porous and a granular material are taken into account by different intrinsic parameters that characterize each material [38]. The pore size for a granular material can for example be related to a distribution close to log-normal [39], or can also be calculated by assuming a packing of spheres [40]–[42]. The study of acoustic properties of light and non-cohesive granular materials, such as polystyrene expanded beads, is however not found in literature.

In this paper, a model based on Biot's theory is adapted to light and non-cohesive granular materials. It is indeed necessary to take into account the solid phase and its interactions with the fluid phase to describe properly the global behavior since the lightness of beads and the point contact between beads does not allow to consider a rigid skeleton. However, the solid phase of granular materials is not a continuous medium and cannot be modelled by a standard continuous elastic solid. Indeed, according to the kind of solicitation, granular materials can behave more like solid (within plasticity theories), or more like fluid. Basically, three behaviours can be distinguished: quasi–static behaviour, rapid granular flow behaviour, and intermediate behaviour. The quasi–static regime occurs at low shear rates where friction between beads is predominant. In this case, shear stresses are proportional to inter-particle pressure and are independent of the shear rate: it can then be related to Coulomb's theory and Hertz's theory [43]. The rapid granular flow regime occurs at high shear rates with collisional interactions between particles. Finally, recent works on granular materials show that a simple model using a macroscopic coefficient of friction could be used to describe the granular material behaviour for the quasi–static regime, and also for rapid granular flows. A continuum constitutive model for cohesionless granular flows is hence described in [44] with a stress tensor presented in Eq. (6). P_{ij} is a diagonal tensor that takes into account the anisotropy of static normal stresses. In the absence of motion, the three components are the static normal stresses

$$\sigma_{ij} = -P_{ij} + \tau_{ij}. \tag{6}$$

τ_{ij} is the deviatory stress tensor that can be expressed by considering a Bingham fluid. In the case of 1D simple shear flow, it yields the following simplification given in Eq. (7):

$$\tau_{ij} = \mu_{\mathrm{B}}\dot{\gamma}_{ij}. \tag{7}$$

The macroscopic coefficient of friction μ_{B} is then given by Eq. (8), where P_{g} is the pressure of the granular phase, μ^{*}_{min} is the static coefficient of friction, $\dot{\gamma}$ is the second invariant of the rate of strain tensor: $\dot{\gamma} = \sqrt{0.5\dot{\gamma}_{ij}\dot{\gamma}_{ij}}$, b is a coefficient of proportionality, d is the particle diameter, and ρ_{p} is the particle density. This macroscopic coefficient of friction enables to take into account the frictional and collisional phenomena,

$$\mu_{\mathrm{B}} = \frac{\mu^{*}_{\mathrm{min}} P_{\mathrm{g}}}{\dot{\gamma}} + bd\sqrt{\rho_{\mathrm{p}}\, P_{\mathrm{g}}}. \tag{8}$$

The idea developed in this work is to adapt this continuum constitutive model for light and non-cohesive granular materials in Biot's model. Resulting changes in Biot's model lead to a simplified fluid–fluid model that allows to improve the efficiency of numerical methods used to characterize such materials.

In the following, simplifications in Biot's poroelasticity equations are detailed, and lead to a fluid–fluid model with a pressure formulation (P_s, P_f). A solution is then presented for a 1D problem, and the surface impedance of a poro-granular material sample subjected to normal incidence plane waves is calculated, allowing the determination of intrinsic material parameters obtained by fitting this calculated surface impedance to a measured one. Comparisons are made with data found in literature and direct measurements with a micro-tomograph. Finally, a study on thermal and viscous dissipations is presented and illustrated by pressures and velocities distributions in the poro-granular material sample.

3 Continuum constitutive model for solid phase

The continuum constitutive model used to describe the solid phase in Biot's model is described here. It is based on the continuum constitutive model for cohesionless granular flows detailed in [44]. Two simplifications are made from this model. First, static normal stresses are considered isotropic as in [45]. The stress tensor is then given by Eq. (9),

$$\sigma_{ij} = -P_g \delta_{ij} + \mu_B \dot{\gamma}_{ij}. \tag{9}$$

The pressure inside the granular material can then be divided into a static load P_0 and a small dynamic load δP such as $P_g = P_0 + \delta P$. Since no preload is applied on the granular material, P_0 is set to zero. On the other hand, the macroscopic coefficient of friction μ_B given in Eq. (8) varies with the pressure P_g. A small dynamic load implies therefore a small macroscopic coefficient of friction μ_B. Moreover, the macroscopic coefficient of friction in Eq. (8) can be split into a static coefficient of friction (first term), and a dynamic coefficient of friction (second term). The shear stress due to the static coefficient can be neglected since no preload is applied, and the part due to the dynamic coefficient is even smaller for light and small beads and for low shear rates. Finally, the stress tensor for the granular phase reads

$$\sigma_{ij} = -P_g \delta_{ij}. \tag{10}$$

Of course the proposed simplifications cannot be used for all types of poro-granular materials but only for light non-cohesive ones. The quality of the proposed approximation will be checked in the following by comparing with experimental results in the particular case of 1D problems.

4 Fluid/fluid model

In this Section, Biot's model is adapted to light and non-cohesive poro-granular materials. The continuum constitutive model given in Eq. (10) is used for the solid granular phase. This significant simplification leads to a fluid/fluid model that can be used to characterize light and non-cohesive poro-granular materials.

4.1 Assumption on solid phase shear stress and fluid like behavior of beads

The main idea used to adapt Biot's model with the continuum constitutive model given in Eq. (10) for light and non-cohesive poro-granular materials is to assume the solid phase shear stress to be negligible, and a fluid like behavior of beads. Indeed it does not exist a real cohesion between beads at the macroscopic level and the rigidity is essentially due to contact forces

between beads. Thereby, in first approximation shear forces are neglected compared to normal contact forces, suggesting that macroscopic beads' behavior is comparable to a perfect fluid. This leads to a modified Biot's model taking into account two interacting fluid phases.

4.2 Simplification of strain–stress relations

Introducing the continuum constitutive model given in Eq. (10) into Biot's equations leads to neglecting the shear stresses in Eq. (2), and assuming a fluid like behavior of beads. The solid stress tensor can then be directly linked to the trace of the solid strain tensor thanks to an equivalent solid compressibility modulus K_b. The new set of equations is written in Eq. (11), with elastic coefficients given by: $P = K_\mathrm{b} + Q\frac{1-\phi}{\phi},\ Q = (1-\phi)K_\mathrm{f},\ R = \phi K_\mathrm{f}$:

$$\begin{aligned} \underline{\underline{\sigma}}^\mathrm{s} &= Ptr(\underline{\underline{\varepsilon}}^\mathrm{s})\underline{\underline{1}} + Qtr(\underline{\underline{\varepsilon}}^\mathrm{f})\underline{\underline{1}}, \\ \underline{\underline{\sigma}}^\mathrm{f} &= Rtr(\underline{\underline{\varepsilon}}^\mathrm{f})\underline{\underline{1}} + Qtr(\underline{\underline{\varepsilon}}^\mathrm{s})\underline{\underline{1}}. \end{aligned} \tag{11}$$

The two equations are similar, and can be related to a fluid/fluid behavior.

4.3 (P_s, P_f) formulation

The fluid stress tensor can be expressed by the fluid pressure $P_\mathrm{f} : \underline{\underline{\sigma}}^\mathrm{f} = -P_\mathrm{f}(x,y,z)\underline{\underline{1}}$. As the shear stress has been neglected in the solid phase, a similar expression can also be written for the solid phase thanks to an equivalent solid pressure $P_\mathrm{s} : \underline{\underline{\sigma}}^\mathrm{s} = -P_\mathrm{s}(x,y,z)\underline{\underline{1}}$. In the following, the spatial parameters x, y and z will be omitted. Using these two stress tensors in Eq. (4), the expressions of solid and fluid displacements are re-written in Eq. (12):

$$\begin{aligned} \vec{u}_\mathrm{s} &= \frac{\rho_{22}\overrightarrow{\mathrm{grad}}(P_\mathrm{s}) - \rho_{12}\overrightarrow{\mathrm{grad}}(P_\mathrm{f}) - \rho_{22}\vec{f}^{\,\mathrm{s}}_{v} + \rho_{12}\vec{f}^{\,\mathrm{f}}_{v}}{\left(\rho_{11}\rho_{22} - \rho_{12}^2\right)\omega^2}, \\ \vec{u}_\mathrm{f} &= \frac{\rho_{11}\overrightarrow{\mathrm{grad}}(P_\mathrm{f}) - \rho_{12}\overrightarrow{\mathrm{grad}}(P_\mathrm{s}) - \rho_{11}\vec{f}^{\,\mathrm{f}}_{v} + \rho_{12}\vec{f}^{\,\mathrm{s}}_{v}}{\left(\rho_{11}\rho_{22} - \rho_{12}^2\right)\omega^2}. \end{aligned} \tag{12}$$

In Eq. (11), strain tensors can be related to local displacements found in Eq. (12) thanks to $tr(\underline{\underline{\varepsilon}}) = \mathrm{div}(\vec{u})$, and give the pressure formulation (P_s, P_f) in Eq. (13):

$$\begin{aligned} &-\left(\left(\rho_{11}\rho_{22} - \rho_{12}^2\right)\omega^2\right)P_\mathrm{s} = (\rho_{22}P - \rho_{12}Q)\Delta P_\mathrm{s} + (\rho_{11}Q - \rho_{12}P)\Delta P_\mathrm{f} \\ &\quad + (\rho_{12}Q - \rho_{22}P)\mathrm{div}\left(\vec{f}^{\,\mathrm{s}}_{v}\right) + (\rho_{12}P - \rho_{11}Q)\mathrm{div}\left(\vec{f}^{\,\mathrm{f}}_{v}\right), \\ &-\left(\left(\rho_{11}\rho_{22} - \rho_{12}^2\right)\omega^2\right)P_\mathrm{f} = (\rho_{11}R - \rho_{12}Q)\Delta P_\mathrm{f} + (\rho_{22}Q - \rho_{12}R)\Delta P_\mathrm{s} \\ &\quad + (\rho_{12}Q - \rho_{11}R)\mathrm{div}\left(\vec{f}^{\,\mathrm{f}}_{v}\right) + (\rho_{12}R - \rho_{22}Q)\mathrm{div}\left(\vec{f}^{\,\mathrm{s}}_{v}\right). \end{aligned} \tag{13}$$

Assuming now that there are no local sources inside solid and fluid phases, Eq. (13) can be simplified by Eq. (14). This new formulation is very simple compared to the classical Biot's formulation since it only uses two degrees of freedom (P_s and P_f),

$$\begin{aligned} &[A\Delta\mathbf{P_s} + \mathbf{P_s}] + B\Delta\mathbf{P_f} = 0, \\ &[C\Delta\mathbf{P_f} + \mathbf{P_f}] + D\Delta\mathbf{P_s} = 0 \end{aligned} \tag{14}$$

with $A = \frac{\rho_{22}P - \rho_{12}Q}{\left(\rho_{22}\rho_{11} - \rho_{12}^2\right)\omega^2}$; $B = \frac{\rho_{11}Q - \rho_{12}P}{\left(\rho_{22}\rho_{11} - \rho_{12}^2\right)\omega^2}$; $C = \frac{\rho_{11}R - \rho_{12}Q}{\left(\rho_{22}\rho_{11} - \rho_{12}^2\right)\omega^2}$; $D = \frac{\rho_{22}Q - \rho_{12}R}{\left(\rho_{22}\rho_{11} - \rho_{12}^2\right)\omega^2}$.

5 One dimensional fluid/fluid model and solutions

In this Section, the case of a tube filled with a poro-granular material excited by a plane wave at normal incidence is studied (see Fig. 1). The restriction to one dimension of general Eq. (14) is necessary to describe this problem [cf. Eq. (15)]. Fluid and solid displacements in Eq. (12) are also simplified to one dimension in Eq. (16). This 1D study does not allow to verify the validity of the neglecting shear stresses assumption. However, the simplicity of the (P_{s}, P_{f}) formulation that is also valid for 3D problems is hence presented before to be adapted on more complex structures using modal expansion on the three directions,

$$\begin{aligned}\left[A\tfrac{d^2P_{\mathrm{s}}(x)}{dx^2}+P_{\mathrm{s}}(x)\right]+B\tfrac{d^2P_{\mathrm{f}}(x)}{dx^2}=0,\\ \left[C\tfrac{d^2P_{\mathrm{f}}(x)}{dx^2}+P_{\mathrm{f}}(x)\right]+D\tfrac{d^2P_{\mathrm{s}}(x)}{dx^2}=0,\end{aligned} \tag{15}$$

$$\begin{aligned}u_{\mathrm{s}}^x&=\frac{1}{(\rho_{11}\rho_{22}-\rho_{12}^2)\omega^2}\left(\rho_{22}\frac{dP_{\mathrm{s}}}{dx}-\rho_{12}\frac{dP_{\mathrm{f}}}{dx}\right),\\ u_{\mathrm{f}}^x&=\frac{1}{(\rho_{11}\rho_{22}-\rho_{12}^2)\omega^2}\left(\rho_{11}\frac{dP_{\mathrm{f}}}{dx}-\rho_{12}\frac{dP_{\mathrm{s}}}{dx}\right).\end{aligned} \tag{16}$$

A rigid boundary condition is taken at $x = L$, and excitation is applied at $x = 0$ with an excitation pressure P_{exc}. These standard boundary conditions are given in Eq. (17):

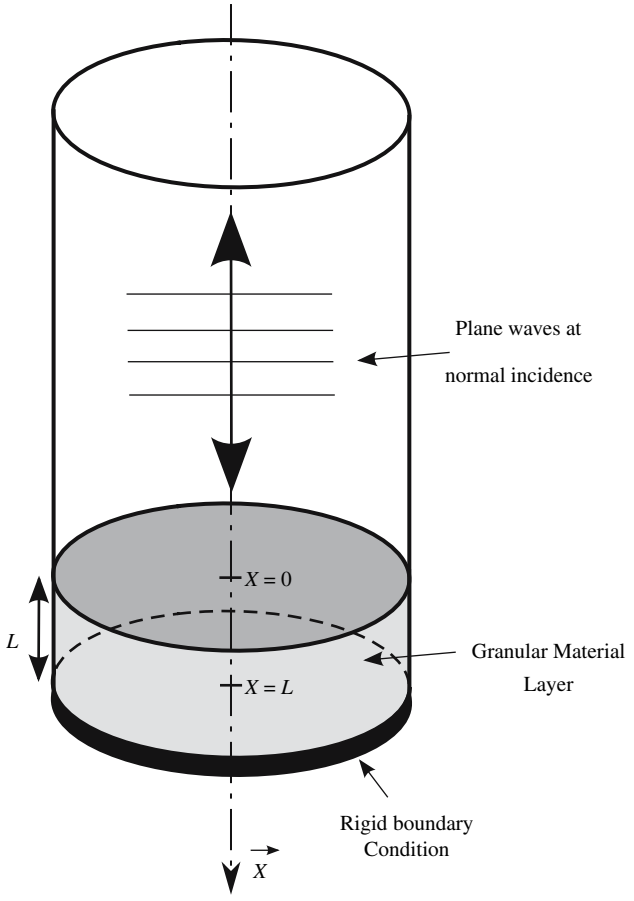

Fig. 1. Description of a poro-ganular material sample subjected to plane waves excitation

$$
\begin{aligned}
&P_{\mathrm{s}}(0) = (1-\phi)P_{\mathrm{exc}},\\
&P_{\mathrm{f}}(0) = (\phi)P_{\mathrm{exc}},\\
&u_{\mathrm{s}}(L) = u_{\mathrm{f}}(L) = 0.
\end{aligned}
\tag{17}
$$

Solutions of the problem are expected in the following form: $P_{\mathrm{s}}\ (x) = e^{jkx}$ and $P_{\mathrm{f}}\ (x) = e^{jkx}$. Replacing these expressions in Eq. (15) lead to Eq. (18):

$$
\begin{bmatrix} -k^2A+1 & -k^2B \\ -k^2D & -k^2C+1 \end{bmatrix} \begin{Bmatrix} P_{\mathrm{s}} \\ P_{\mathrm{f}} \end{Bmatrix} = 0. \tag{18}
$$

To avoid the solution $P_{\mathrm{s}} = P_{\mathrm{f}} = 0$, the determinant of the system must be zero. This condition leads to four wave numbers (k_1, $-k_1$, k_2, and $-k_2$) given by Eq. (19),

$$
\begin{aligned}
k_1^2 &= \frac{A+C-\sqrt{(A+C)^2-4(AC-BD)}}{2(AC-BD)},\\
k_2^2 &= \frac{A+C+\sqrt{(A+C)^2-4(AC-BD)}}{2(AC-BD)}.
\end{aligned}
\tag{19}
$$

Two mode shapes vectors V_1 and V_2 are related to wave numbers k_1 and k_2 [cf. Eq. (20)],

$$
V_1 = \begin{pmatrix} \frac{Bk_1^2}{1-Ak_1^2} \\ 1 \end{pmatrix}; \quad V_2 = \begin{pmatrix} \frac{Bk_2^2}{1-Ak_2^2} \\ 1 \end{pmatrix}. \tag{20}
$$

Solid and fluid pressures are then obtained by adding the two modal contributions, as presented in Eq. (21), where q_1 and q_2 are defined as: $q_1 = a_1e^{jk_1x} + \alpha_2e^{-jk_1x}$, $q_2 = \beta_1e^{jk_2x} + \beta_2e^{-jk_2x}$, and constants α_1, α_2, β_1, β_2 depend on the boundary conditions:

$$
\begin{Bmatrix} P_{\mathrm{s}} \\ P_{\mathrm{f}} \end{Bmatrix} = \begin{bmatrix} \frac{Bk_1^2}{1-Ak_1^2} & \frac{Bk_2^2}{1-Ak_2^2} \\ 1 & 1 \end{bmatrix} \begin{Bmatrix} q_1 \\ q_2 \end{Bmatrix}. \tag{21}
$$

Taking into account the boundary conditions Eq. (17) gives the following constants:

$$
\alpha_1 = \frac{(1-\phi)P_{\mathrm{exc}} - \phi\frac{Bk_2^2}{1-Ak_2^2}P_{\mathrm{exc}}}{\left(\frac{Bk_1^2}{1-Ak_1^2} - \frac{Bk_2^2}{1-Ak_2^2}\right)(1+e^{2jk_1L})}, \qquad \beta_1 = \frac{(1-\phi)P_{\mathrm{exc}} - \phi\frac{Bk_1^2}{1-Ak_1^2}P_{\mathrm{exc}}}{\left(\frac{Bk_2^2}{1-Ak_2^2} - \frac{Bk_1^2}{1-Ak_1^2}\right)(1+e^{2jk_2L})},
$$

$$
\alpha_2 = \alpha_1e^{2jk_1L}, \qquad \beta_2 = \beta_1e^{2jk_1L}.
$$

Solid and fluid pressures along the x-axis can therefore be determined [see Eq. (22)], and using Eq. (16) solid and fluid displacements can also be determined,

$$
\begin{aligned}
P_{\mathrm{s}} = &\frac{k_1^2}{1-Ak_1^2}\frac{(1-\phi)P_{\mathrm{exc}} - \phi\frac{Bk_2^2}{1-Ak_2^2}P_{\mathrm{exc}}}{\left(\frac{k_1^2}{1-Ak_1^2} - \frac{k_2^2}{1-Ak_2^2}\right)(1+e^{2jk_1L})}\left(e^{jk_1x} + e^{2jk_1L-jk_1x}\right)\\
&+\frac{k_2^2}{1-Ak_2^2}\frac{(1-\phi)P_{\mathrm{exc}} - \phi\frac{Bk_1^2}{1-Ak_1^2}P_{\mathrm{exc}}}{\left(\frac{k_2^2}{1-Ak_2^2} - \frac{k_1^2}{1-Ak_1^2}\right)(1+e^{2jk_2L})}\left(e^{jk_2x} + e^{2jk_1L-jk_2x}\right),
\end{aligned}
$$

$$P_{\mathrm{f}} = \frac{(1-\phi)P_{\mathrm{exc}} - \phi\frac{Bk_2^2}{1-Ak_2^2}P_{\mathrm{exc}}}{\left(\frac{Bk_1^2}{1-Ak_1^2} - \frac{Bk_2^2}{1-Ak_2^2}\right)(1+e^{2jk_1L})}\left(e^{jk_1x} + e^{2jk_1L-jk_1x}\right) + \frac{(1-\phi)P_{\mathrm{exc}} - \phi\frac{Bk_1^2}{1-Ak_1^2}P_{\mathrm{exc}}}{\left(\frac{Bk_2^2}{1-Ak_2^2} - \frac{Bk_1^2}{1-Ak_1^2}\right)(1+e^{2jk_2L})}\left(e^{jk_2x} + e^{2jk_1L-jk_2x}\right). \tag{22}$$

6 Acoustical inverse measurement to determine the intrinsic parameters of a poro-granular material

This Section presents the method used to characterize a poro-granular material. The material studied here is made of expanded polystyrene beads having a density of 19 g L^{-1}. Results obtained by this method are presented and then compared with other measurements.

6.1 Principle

The theoretical expression of the surface impedance can be derived from the results of the previous Section. It is defined as the ratio of exciting pressure to the average velocity of both phases. The surface impedance expression is then obtained with Eq. (23),

$$Z = \frac{P_{\mathrm{exc}}}{j\omega(\phi u_{\mathrm{f}}(0) + (1-\phi)u_{\mathrm{s}}(0))}. \tag{23}$$

The aim of the acoustical inverse measurement is to find the best set of characteristic parameters SP to minimize differences between theoretical and experimental values of surface impedance (respectively, Z^{th} and Z^{exp}). Real and imaginary parts of surface impedance are considered and the root least mean square method is used to evaluate the differences. Minimization is done over several samples of different thickness "e", and over several frequencies "f". A cost function is thus defined by Eq. (24):

$$f_{\mathrm{cost}}(SP) = \sum_e \sum_f \left[\Re e\left(Z^{\mathrm{th}}(SP,f,e)\right) - \Re e\left(Z^{\mathrm{exp}}(f,e)\right)\right]^2 \ldots + \left[\Im m\left(Z^{\mathrm{th}}(SP,f,e)\right) - \Im m\left(Z^{\mathrm{exp}}(f,e)\right)\right]^2. \tag{24}$$

An optimization tool is then necessary to find the best set of parameter SP that minimizes the cost function as for example an hybrid algorithm combining a gradient method with a genetic algorithm. Matlab optimization toolbox and genetic algorithm toolbox have been employed to realize this kind of optimization.

6.2 Surface impedance measurement

Acoustic properties of several samples of expanded polystyrene beads (diameter $\sim$1.5 mm) have been measured using a two-microphones impedance tube BK 4206 according to the norm ISO 10534-2 in the frequency range 200–1,600 Hz. The standard measurement set-up with two microphones is presented in Fig. 2. It is placed vertically to keep the poro-granular material at the bottom end of the tube.

It is important to notice that acoustic properties measurements are subjected to several kinds of uncertainties. Specific studies are necessary to estimate these uncertainties and can be found in [46]–[48]. In the following, error bars are not presented in the results for more clarity.

Absorption coefficients obtained are presented for two particular thicknesses on Fig. 3. A maximum of absorption occurs theoretically when the sample thickness is equal to a quarter acoustic wavelength. However, as fluid properties are modified by the poro-granular media, a change in the acoustic wavelength is also expected in the fluid phase. This point is more detailed in Sect. 8 where pressures and velocities distributions in the sample are presented for different frequencies.

Associated surface impedances are presented for two particular thicknesses on Fig. 4. The real part is related to the power dissipated inside the material (cf. Sect. 7). However, absorption and dissipation are not maximum at the same frequency because absorption takes also into account reflexion at the surface sample. When the surface impedance is equal to air impedance $\rho_0\, c$, then the reflexion is null, and absorption is maximum.

6.3 Results

Minimization of the cost function given by Eq. (24) and application to samples of expanded polystyrene beads ($\rho_s = 19$ g L^{-1}) lead to the results presented in Table 1. Values of parameters obtained are coherent with other data. Air flow resistivity can also be calculated from viscous permeability and leads to a very low resistivity ($2{,}000$ N m^{-4} s), that is also coherent with reality. It is however important to notice that the set of optimized parameters is not unique. Therefore, particular care is needed to define constraints on each parameter so that they could agree well with the microstructure considered.

The discussion about solid phase elasticity is also a particular point. Some order of magnitude can be reminded: Young's modulus of a polystyrene material is around $3{,}000$ MPa, and that of expanded polystyrene is around 10–30 MPa. For a granular sample of EPS beads, Young's modulus is much lower since a punctual contact between beads is introduced, and since also there is no preload on the sample. Hertz's theory for punctual contact gives a non-linear law between the force applied and the local deformation. To get a linear law and to be able to define an elastic equivalent modulus, it is

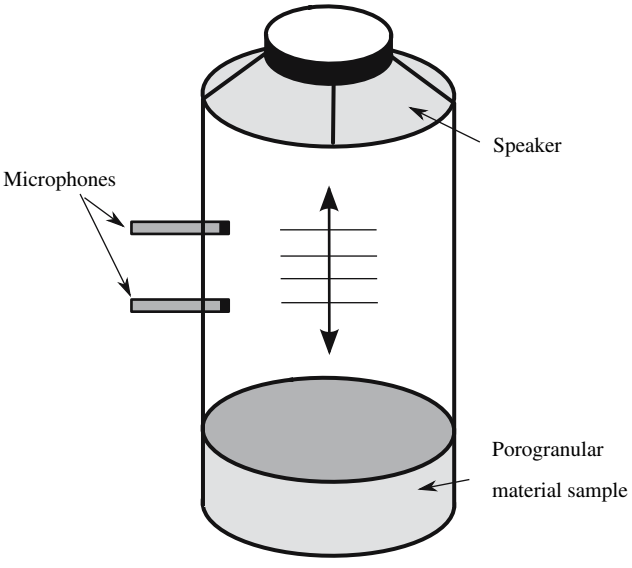

Fig. 2. Experimental setup description

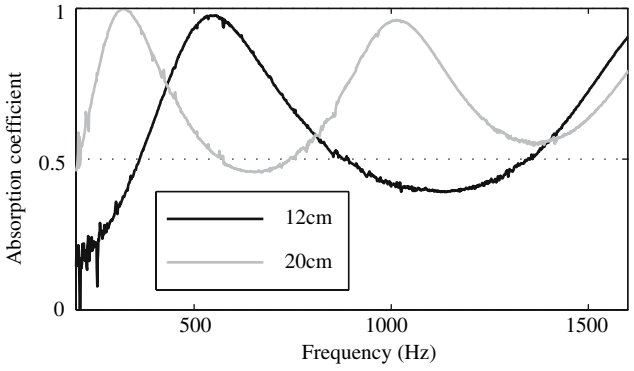

Fig. 3. Absorption coefficient of poro-granular material measured on two samples of different thicknesses

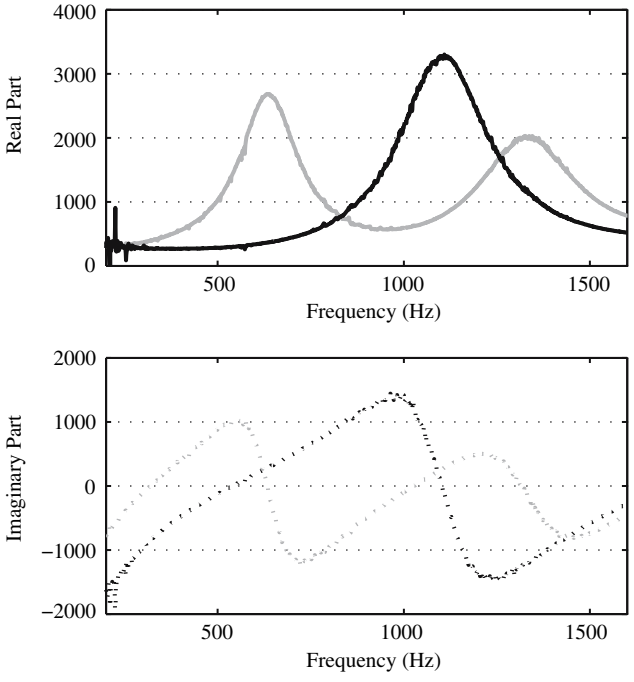

Fig. 4. Surface impedances (Pa m^{-1} s) of a poro-granular material measured on two samples of different thicknesses. *Black lines* sample of 12 cm, *grey lines* sample of 20 cm, *dotted lines* imaginary parts, *solid lines* real parts

Table 1. Values of characteristics intrinsic parameters obtained by inverse measurement for a poro-granular material

Parameter	Value
ϕ	0.41
α_∞	1.2855
k_0	9.2 9 10^{-9} m^2
Λ	0.20 mm
Λ'	0.34 mm
K_b	10^4 $(1 + 0.18i)$ Pa

necessary to consider a static deformation and small dynamic perturbations around this static deformation. The elastic equivalent modulus is then related to the static deformation. If the preload is small, then the static deformation and the elastic equivalent modulus are also small. Finally, the bulk

modulus is lower than Young's modulus and can therefore be very small for a sample of EPS beads. Our result is still low but even for standard materials such as plastic foam Recticel, low values can be found (1.1 MPa). Hence for particularly light and non-cohesive granular material, it does not seem unrealistic to have lower values. It is also important to notice that an increase up to 0.2 MPa does not change significantly surface impedances calculated on the considered frequency band, while reducing it has no effect at all. It can therefore be concluded that effects of solid phase elasticity on surface impedance are negligible compared to those of fluid phase elasticity. The value of solid bulk modulus obtained is thus not really relevant being given that the parameter is not significant. Finally, the last point that is also important to understand the very low value of the skeleton bulk modulus is the non-linear behavior of a unilateral contact between beads due to a light and non-cohesive material. This unilateral contact reduces of course the effects of solid phase elasticity and leads inevitably to a very low skeleton bulk modulus.

Since the solid phase bulk modulus (around 10–30 MPa) is much higher than the skeleton bulk modulus (around 0.01–0.2 MPa) and also much higher than the one of air (0.142 MPa), simplified expressions of the elastic coefficients P, Q and R given in Eq. (3) can therefore be used.

Finally, comparison of surface impedances measured and calculated from optimized parameters is given in Fig. 5. A very good agreement between the model and the measure is obtained. Hence, parameters given by inverse measurements can be considered as reliable, and the fluid/fluid model as efficient to characterize the vibroacoustic behavior of this poro-granular material.

6.4 Comparisons

In [40], air-saturated random packings of beads were studied, and values of characteristic intrinsic parameters are given in Table 2. These parameters can be compared with those obtained for expanded polystyrene beads in Table 1 since the microstructure is similar (beads with same size properties: diameter $\sim$1.5 mm). Differences to intrinsic parameters in Table 1 are however not negligible, but can be explained by a small difference in the standard deviation of beads' diameter. Thereby, although the results are slightly different, the order of magnitude shows that the intrinsic parameters found are in good agreement with the microstructure geometry. One has however to remind that the acoustical inverse measurement is not aimed to give precise results, but a good assessment of intrinsic parameters value.

A direct measurement is also a good way to assess the accuracy of values obtained by inverse measurements. Some parameters are very easy to get from microstructure geometry. Hence, with pictures given by 3D microtomography, it is possible to get porosity and tortuosity. However, expanded polystyrene does not absorb X-rays sufficiently, and identical glass beads (diameter $\sim$1.5 mm) have therefore been used instead, and lead to the microstructure presented on Fig. 6. Porosity and tortuosity measured from this microstructure are, respectively: $\phi = 0.36$, $\alpha_\infty = 1.37$. Inverse measurements can thus be considered as reliable since results are very close to direct measurements.

7 Viscous and thermal dissipations

In order to highlight viscous and thermal dissipations that take place in each phase of the poro-granular sample, a power balance is necessary. In that aim, poroelasticity equations [Eq. (4)] are multiplied by solid and fluid conjugate velocities and integrated over the sample volume, and lead to Eq. (25).

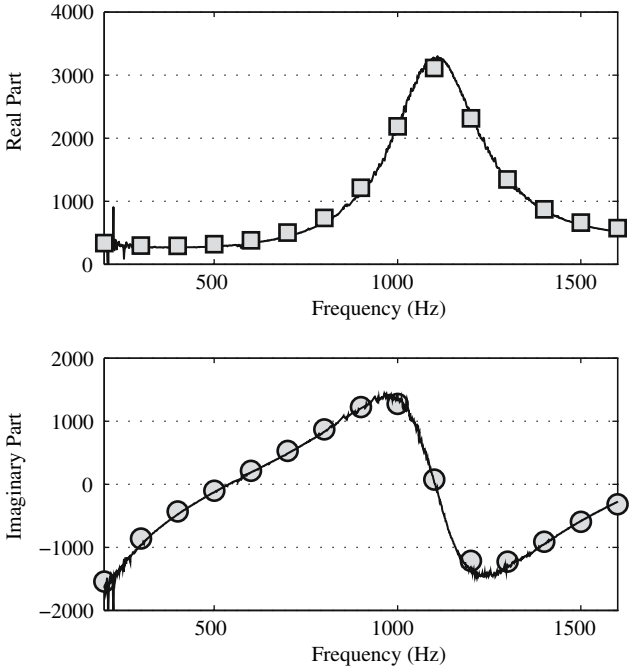

Fig. 5. Comparison between theoretical and experimental surface impedances of a 12 cm sample of poro-granular material – *solid lines* measured impedance, *markers* fitted theoretical impedance

Table 2. Values of characteristics intrinsic parameters given by Allard et al. [40] for an air-saturated random packing of beads

Parameter	Value
ϕ	0.4
α_∞	1.37
k_0	$1.5\ 9\ 10^{-9}$ m^2
Λ	0.09 mm
Λ'	0.32 mm

$$\begin{aligned}
\int_V \left(-\overrightarrow{\text{grad}}(P^{\text{s}}) \cdot \vec{V}^{\text{s}*}\right) dV &= \int_V \left(\rho_{11}\vec{\gamma}^{\text{s}} \cdot \vec{V}^{\text{s}*} + \rho_{12}\vec{\gamma}^{\text{f}} \cdot \vec{V}^{\text{s}*}\right) dV, \\
\int_V \left(-\overrightarrow{\text{grad}}(P^{\text{f}}) \cdot \vec{V}^{\text{f}*}\right) dV &= \int_V^L \left(\rho_{22}\vec{\gamma}^{\text{f}} \cdot \vec{V}^{\text{f}*} + \rho_{12}\vec{\gamma}^{\text{s}} \cdot \vec{V}^{\text{f}*}\right) dV.
\end{aligned} \tag{25}$$

The study is now simplified to 1D case, and integration by parts is used to write the power balance in Eq. (26),

$$\begin{aligned}
\left(P^{\text{s}} S \cdot V_x^{\text{s}*}\right)\big|_{x=0} &= -\int_0^L \left(P^{\text{s}} \cdot \frac{d\left(V_x^{\text{s}*}\right)}{dx}\right) S dx + \int_0^L \left(\rho_{11}\gamma_x^{\text{s}} \cdot V_x^{\text{s}*} + \rho_{12}\gamma_x^{\text{f}} \cdot V_x^{\text{s}*}\right) S dx, \\
\left(P^{\text{f}} S \cdot V_x^{\text{f}*}\right)\big|_{x=0} &= -\int_0^L \left(P^{\text{f}} \cdot \frac{d\left(V_x^{\text{f}*}\right)}{dx}\right) S dx + \int_0^L \left(\rho_{22}\gamma_x^{\text{f}} \cdot V_x^{\text{f}*} + \rho_{12}\gamma_x^{\text{s}} \cdot V_x^{\text{f}*}\right) S dx.
\end{aligned} \tag{26}$$

Several terms appear in these expressions: real parts of the left hand sides are the total dissipations in solid and fluid phases, while real parts of the right hand sides are internal dissipations (thermal and viscous);

$Re\left(\left(P^{\mathrm{s}}S \cdot V_x^{\mathrm{s}*}\right)\big|_{x=0}\right)$: total dissipations in solid phase

$-\int_0^L Re\left(P^{\mathrm{s}} \cdot \frac{d\left(V_x^{\mathrm{s}*}\right)}{dx}\right) Sdx$: thermal dissipations in solid phase .

$\int_0^L Re\left(\rho_{11}\gamma_x^{\mathrm{s}} \cdot V_x^{\mathrm{s}*} + \rho_{12}\gamma_x^{\mathrm{f}} \cdot V_x^{\mathrm{s}*}\right) Sdx$: viscous dissipations in solid phase

$Re\left(\left(P^{\mathrm{f}}S \cdot V_x^{\mathrm{f}*}\right)\big|_{x=0}\right)$: total dissipations in fluid phase

$-\int_0^L Re\left(P^{\mathrm{f}} \cdot \frac{d\left(V_x^{\mathrm{f}*}\right)}{dx}\right) Sdx$: thermal dissipations in fluid phase .

$\int_0^L Re\left(\rho_{11}\gamma_x^{\mathrm{f}} \cdot V_x^{\mathrm{f}*} + \rho_{12}\gamma_x^{\mathrm{s}} \cdot V_x^{\mathrm{f}*}\right) Sdx$: viscous dissipations in fluid phase.

The absorption coefficient is then given by the ratio of the total dissipated power to incident acoustic power such as: $\alpha = \Pi_{\mathrm{d}}/\Pi_{\mathrm{i}}$. The dissipated power Π_{d} can be calculated by taking into account only one kind of dissipation (viscous or thermal in solid or fluid phase) in order to highlight the influence of this specific dissipation on the absorption coefficient. The incident power is given by $\Pi_{\mathrm{i}} = P_{\mathrm{i}}^2 S/2\rho_0\, c$, where P_{i} is the pressure magnitude of the incident wave which is related to the excitation pressure by the reflexion coefficient R: $P_{\mathrm{i}}\,(1 + R) = P_{\mathrm{exc}}$. The reflexion coefficient is also related to the surface impedance Z given in Eq. (23) with: $R = (Z - \rho_0\, c)/(Z + \rho_0\, c)$.

The results presented in Figs. 7 and 8 show the influence of viscous and thermal dissipations and solid and fluid dissipations on the absorption coefficient. Below 350 Hz, thermal dissipations are predominant, while above 350 Hz viscous dissipations are predominant. It is also clear that solid dissipations are very small compared to fluid dissipations.

8 Pressures and velocities distribution in the sample

Pressures and velocities distributions in the material sample are presented at three different frequencies to show their influence on the absorption coefficient. Figures 9 and 10 are related to the first absorption peak at 540 Hz. Figures 11 and 12 are related to the frequency $1{,}100$ Hz where absorption is very low. Finally, Figs. 13 and 14 are related to the second peak of absorption at $1{,}720$ Hz.

At 540 and $1{,}720$ Hz, the magnitude of pressures and velocities in each phase is much higher than at $1{,}100$ Hz, and explains a better absorption at those frequencies. Moreover, the maximum of absorption, as expected, occurs when the sample thickness is equal to 1, 3, 5,... quarter wavelength, while the minimum of absorption occurs when the sample thickness is equal to 2, 4, 6,... quarter wavelength. In fact, as discussed in the previous Section, viscous dissipations are preponderant in the studied frequency band. In order to understand the absorption phenomenon, the velocities distribution is thus necessary, and is more important than the pressures distribution. Indeed, when the sample thickness is equal to 1, 3, 5,... quarter wavelength, the velocity response is large at $x = 0$. Therefore, excitation at those frequencies gives high velocities and leads to high absorption

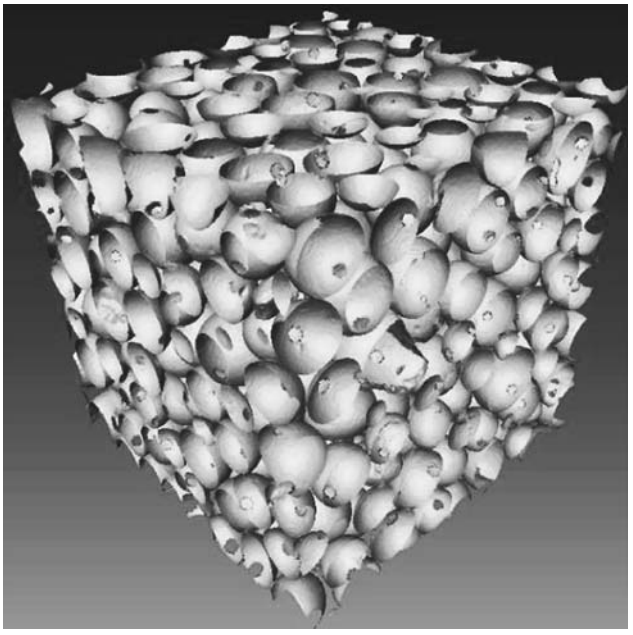

Fig. 6. Microstructure of the poro-granular material obtained by micro-tomography

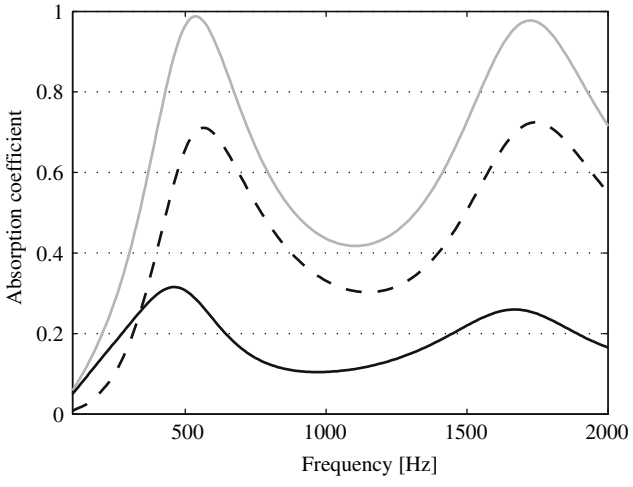

Fig. 7. Influence of viscous (*dotted black line*) and thermal (*solid black line*) dissipations on absorption coefficient (*grey line*) of a 12 cm sample of poro-granular material (see Table 1)

coefficients. On the contrary, when the sample thickness is equal to 2, 4, 6,... quarter wavelength, the velocity response is small at $x = 0$, and the incident wave does not produce high velocity responses.

9 Conclusions

A poro-granular model based on a fluid/fluid description has been presented. The (P_{s}, P_{f}) pressure formulation thus obtained is very simplified compared to classical formulations of Biot's theory.

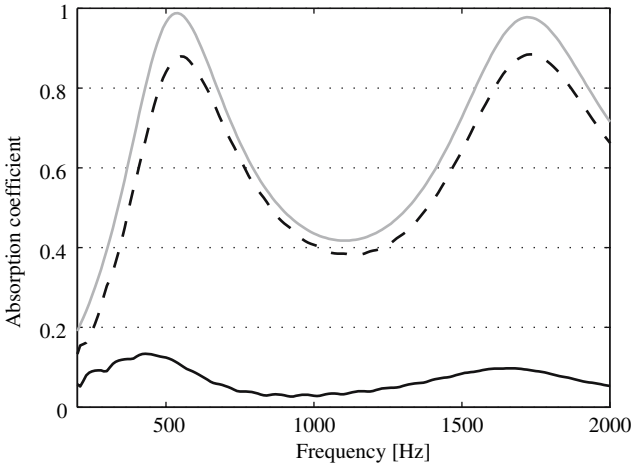

Fig. 8. Influence of fluid (*dotted black line*) and solid (*solid black line*) dissipations on absorption coefficient (*grey line*) of a 12 cm sample of poro-granular material (see Table 1)

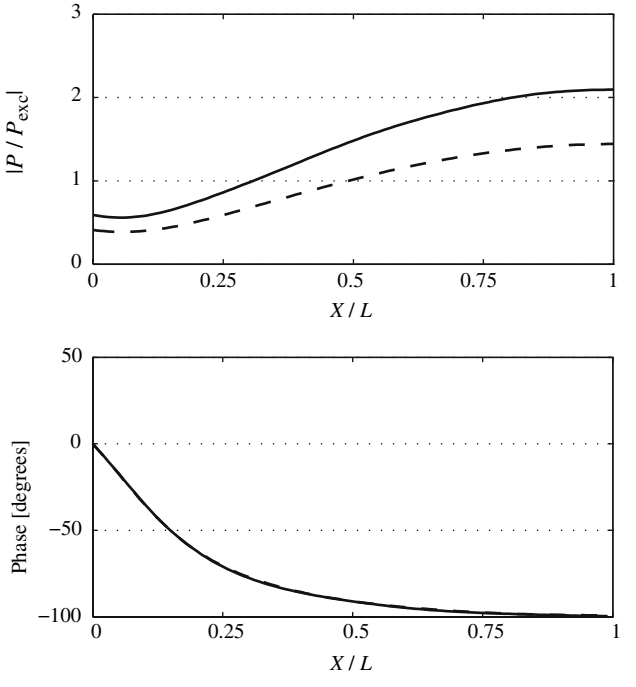

Fig. 9. Fluid (*dotted line*) and solid (*solid line*) pressures in the poro-granular sample material (see Table 1) at 540 Hz in dimensionless form with P_{exc}

Indeed, only two independent variables are necessary to describe the material behavior, instead of four for the (U_{s}, P_{f}) formulation of Biot's model. Moreover, the resolution for the 1D case has been detailed and used to study thermal and viscous dissipations in solid and fluid phases. This 1D study is only aimed to present the simplicity of the formulation. Finally, the characterization of a poro-granular material made of expanded polystyrene granular beads with this model has been realized, and has proved its reliability and accuracy. The next step of this work will be to apply this simplified model to a more complex structure with the same simplicity as described in the 1D case.

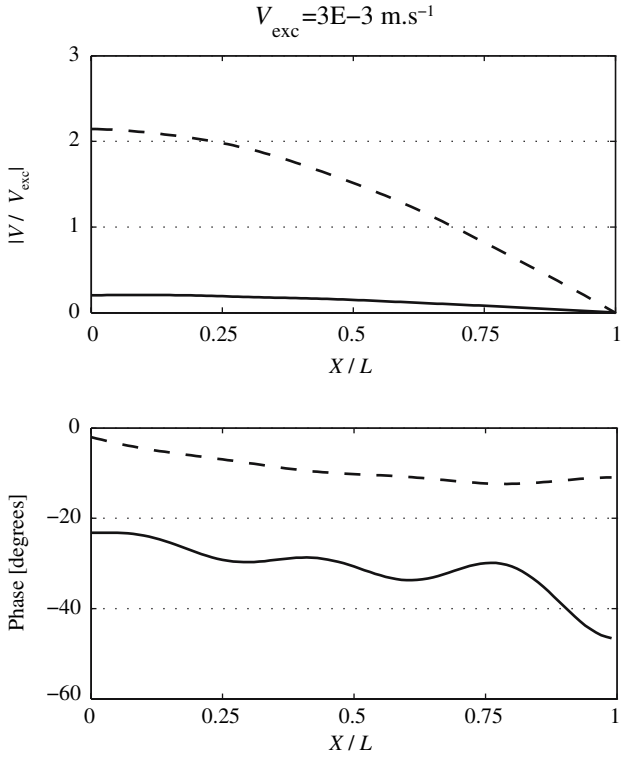

Fig. 10. Fluid (*dotted line*) and solid (*solid line*) velocities in the poro-granular sample (see Table 1) at 540 Hz in dimensionless form with $\mathbf{V_{exc}} = \phi \mathbf{V_f}\,(\mathbf{x} = \mathbf{0}) + (1 - \phi)\,\mathbf{V_s}\,(\mathbf{x} = \mathbf{0})$

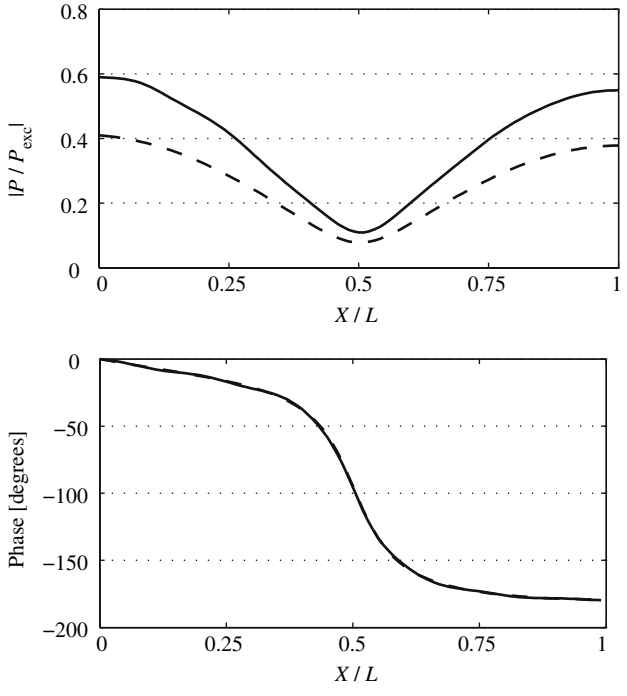

Fig. 11. Fluid (*dotted line*) and solid (*solid line*) pressures in the porogranular sample (see Table 1) at 1,100 Hz in dimensionless form with P_{exc}

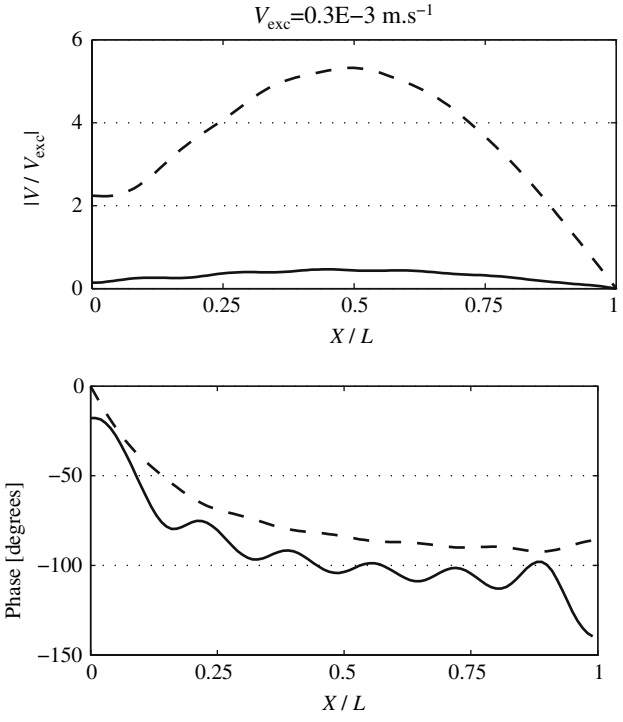

Fig. 12. Fluid (*dotted line*) and solid (*solid line*) velocities in the porogranular sample (see Table 1) at 1,100 Hz in dimensionless form with $\mathbf{V_{exc}} = \phi \mathbf{V_f}\,(\mathbf{x} = \mathbf{0}) + (1 - \phi)\,\mathbf{V_s}\,(\mathbf{x} = \mathbf{0})$

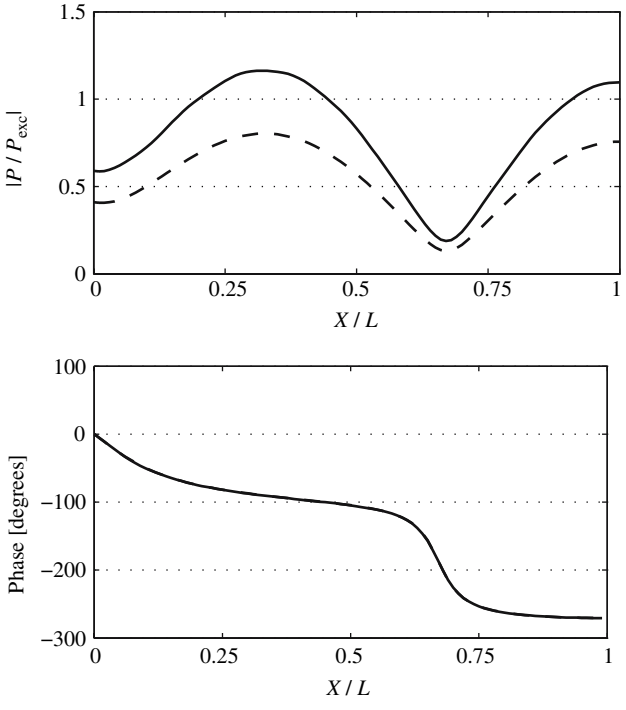

Fig. 13. Fluid (*dotted line*) and solid (*solid line*) pressures in the poro-granular sample (see Table 1) at 1,720 Hz in dimensionless form with P_{exc}

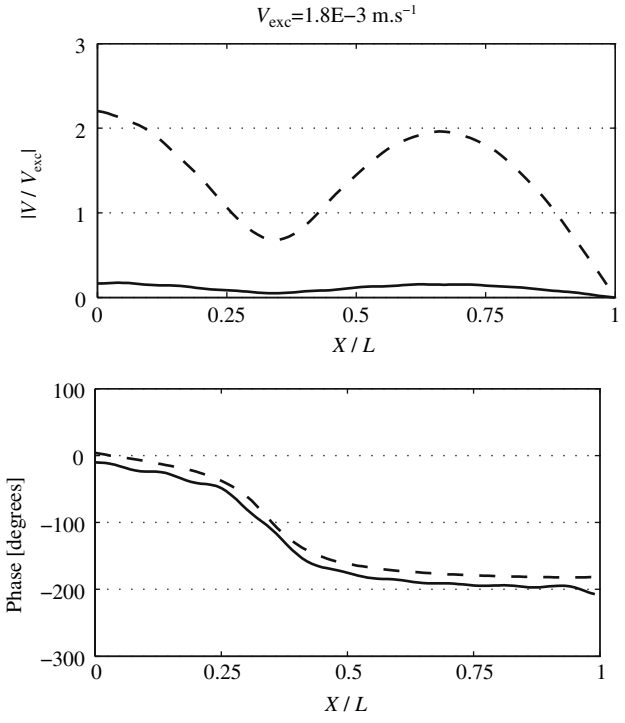

Fig. 14. Fluid (*dotted line*) and solid (*solid line*) velocities in the poro-granular sample (see Table 1) at 1,720 Hz in dimensionless form with $\mathbf{V_{exc}} = \phi \mathbf{V_f}\,(\mathbf{x} = \mathbf{0}) + (1 - \phi)\,\mathbf{V_s}\,(\mathbf{x} = \mathbf{0})$

Acknowledgements

The authors would like to thank Eric Maire and Olivier Caty for their work done on the characterization of the poro-granular microstructure with the 3D-microtomograph.

References

[1] Zwikker, C., Kosten, C.W.: Sound-Absorbing Materials. Elsevier, New York (1949)
[2] Attenborough, K.: Acoustical characteristics of rigid fibrous absorbents and granular media. J. Acoust. Soc. Am. **73**, 785–799 (1983)
[3] Delany, M.E., Bazley, E.N.: Acoustical properties of fibrous asorbent materials. Appl. Acoust. **3** (1970)
[4] Champoux, Y., Allard, J.-F.: Dynamic tortuosity and bulk modulus in air-saturated porous media. J. Appl. Phys. **70**, 1975–1979 (1991)
[5] Johnson, D.L., Plona, T.J., Scala, C.: Tortuosity and acoustic slow waves. Phys. Rev. Lett. **49**, 1840–1844 (1982)
[6] Stinson, M.R., Champoux, Y.: Propagation of sound and the assignment of shape factors in model porous materials having simple pore geometries. J. Acoust. Soc. Am. **91**, 685–695 (1992)
[7] Lafarge, D., Lemarinier, P., Allard, J.F., Tarnow, V.: Dynamic compressibility of air in porous structures at audible frequencies. J. Acoust. Soc. Am. **102**, 1995–2006 (1997)
[8] Allard, J.F.: Propagation of Sound in Porous Media, Modeling Sound Absorbing Materials. Elsevier, London (1993)
[9] Biot, M.A.: The theory of propagation of elastic waves in a fluid saturated porous solid –I. Low-frequency range. J. Acoust. Soc. Am. **28**, 168–178 (1956)
[10] Biot, M.A.: The theory of propagation of elastic waves in a fluid saturated porous solid–II. Higher frequency range. J. Acoust. Soc. Am. **28**, 178–191 (1956)
[11] Biot, M.A.: Generalized theory of acoustic propagation in porous dissipative media. J. Acoust. Soc. Am. **34**, 1254–1264 (1962)

[12] Biot, M.A.: The theory of propagation of elastic waves in a fluid saturated porous solid. J. Acoust. Soc. Am. **28**, 168–191 (1956)
[13] Lauriks, W., Boeckx, L., Leclaire, P., Khurana, P., Kelders, L.: Characterisation of porous acoustic materials. In: SAPEM Proceedings, ENTPE Lyon (2005)
[14] Fellah, Z.E.A., Fellah, M., Sebaa, N., Lauriks, W., Depollier, C.: Measuring flow resistivity of porous materials at low frequencies range via acoustic transmitted waves (l). J. Acoust. Soc. Am. **119**, 1926–1928 (2006)
[15] Perrot, C., Panneton, R., Olny, X.: Computation of the dynamic bulk modulus of acoustic foams. In: SAPEM, ENTPE Lyon (2005)
[16] Iannace, G., Ianiello, C., Maffei, L., Romano, R.: Characteristic impedance and complex wave-number of limestone chips. In: 4th European Conference on Noise Control, Euronoise (2001)
[17] Courtois, T., Falk, T., Bertolini, C.: An acoustical inverse measurement system to determine intrinsic parameters of porous samples. In: SAPEM, ENTPE Lyon (2005)
[18] Dragonetti, R., Ianniello, C., Romano, R.: The use of an optimization tool to search non-acoustic parameters of porous materials. Inter-noise, Prague (2004)
[19] Allard, J.F., Depollier, C., Rebillard, P., Lauriks, W., Cops, A.: Inhomogeneous Biot waves in layered media. J. Appl. Phys. **66**, 2278–2284 (1989)
[20] Atalla, N.: An overview of the numerical modeling of poroelastic materials. In: SAPEM, ENTPE Lyon (2005)
[21] Panneton, R., Atalla, N.: An efficient finite element scheme for solving the three dimensional poroelasticity problem in acoustics. J. Acoust. Soc. Am. **101**, 3287–3298 (1997)
[22] Atalla, N., Panneton, R., Debergue, P.: A mixed displacement–pressure formulation for poroelastic materials. J. Acoust. Soc. Am. **104**, 1444–1452 (1998)
[23] Atalla, N., Hamdi, M.A., Panneton, R.: Enhanced weak integral formulation for the mixed (u, p) poroelastic equations. J. Acoust. Soc. Am. **109**, 3065–3068 (2001)
[24] Debergue, P., Panneton, R., Atalla, N.: Boundary conditions for the weak formulation of the mixed (u,p) poroelasticity problem. J. Acoust. Soc. Am. **106**, 2383–2390 (1999)
[25] Castel, F.: Example of meshing rule for finite element modelling of simple and double porosity materials. In: SAPEM, ENTPE Lyon (2005)
[26] Dazel, O., Sgard, F., Lamarque, C.-H., Atalla, N.: An extension of complex modes for the resolution of finite-element poroelastic problems. J. Sound Vib. **253**, 421–445 (2002)
[27] Dazel, O., Brouard, B., Depollier, C., Griffiths, S.: An alternative Biot's displacement formulation for porous materials. J. Acoust. Soc. Am. **121** (2007)
[28] Hamdi, M.A., Zhang, C., Mebarek, L., Anciant, M., Mahieux, B.: Engineering feedback on numerical simulation of fully trimmed vehicles using modified biot's theory. In: SAPEM, ENTPE, Vaulx en Velin (2005)
[29] Doutres, O., Dauchez, N., Génevaux, J.M., Dazel, O.: Validity of the limp model for porous materials: A criterion based on the Biot theory. J. Acoust. Soc. Am. **122**, 2038–2048 (2007)
[30] Bourinet, J.M.: Approche numérique et expérimentale des vibrations amorties de tubes remplis de matériaux granulaires. Thèse, École Centrale de Nantes (1996)
[31] Bourinet, J.M., Le Houédec, D.: A dynamic stiffness analysis of damped tubes filled with granulars materials. Comput. Struct. **73**, 395–406 (1999)
[32] Saeki, M.: Impact damping with granular materials in a horizontally vibrating system. J. Sound Vib. **251**, 153–161 (2002)
[33] Mao, K., Wang, M.Y., Xu, Z., Chen, T.: Simulation and characterization of particle damping in transient vibrations. American Society of Mechanical Engineers – J. Vib. Acoust. **126** (2004)
[34] Saad, M.H., Adhikari, G., Cardoso, F.: Dem simulation of wave propagation in granular media. Powder Technol. **109**, 222–233 (2000)
[35] Jia, X., Mills, P.: Sound propagation in dense granular materials. Powders and Grains, Kishino (2001)
[36] Voronina, N.N., Horoshenkov, K.V.: A new empirical model for the acoustic properties of loose granular media. Appl. Acoust. **64**, 415–432 (2003)
[37] Attenborough, K.: On the acoustic slow wave in air-filled granular media. J. Acoust. Soc. Am. **81** (1987)
[38] Park, J.: Measurements of the frame acoustic properties of porous and granular materials. J. Acoust. Soc. Am. **118** (2005)
[39] Horoshenkov, K.V., Swift, M.J.: The acoustic properties of granular materials with pore size distribution close to log-normal. J. Acoust. Soc. Am. **110**, Pt. 1 (2001)

[40] Allard, J.F., Henry, M., Tizianel, J., Kelders, L., Lauriks, W.: Sound propagation in air-saturated random packings of beads. J. Acoust. Soc. Am. **102**, 2004–2007 (1998)
[41] Umnova, O., Attenborough, K., Li, K.M.: Cell model calculations of dynamic drag parameters in packings of spheres. J. Acoust. Soc. Am. **107** (2000)
[42] Gasser, S., Paun, F., Bréchet, Y.: Absorptive properties of rigid porous media: Application to face centered cubic sphere packing. J. Acoust. Soc. Am. **117**, Pt. 1 (2005)
[43] Coste, C., Gilles, B.: On the validity of Hertz contact law for granular material acoustics. Eur. Phys. J. B **7**, 155–168 (1999)
[44] Daniel, R.C., Poloski, A.P., Sáez, A.E.: A continuum constitutive model for cohesionless granular flows. Chem. Engng Sci. **62**, 1343–1350 (2007)
[45] Jop, P., Forterre, Y., Pouliquen, O.: A constitutive law for dense granular flows. Nature **441**, 727–731 (2006)
[46] Schultz, T., Shaplak, M., Cattafesta, L.N.: Uncertainty analysis of the two microphone method. J. Sound Vib. **304**, 91–109 (2007)
[47] Bodén, H., Abom, M.: Influence of errors on the two-microphone method for measuring acoustic properties in ducts. J. Acoust. Soc. Am. **79**, 541–549 (1985)
[48] Seybert, A.F., Soenarko, B.: Error analysis of spectral estimates with application to measurement of acoustic parameters using random sound fields in ducts. J. Acoust. Soc. Am. **69**, 1190–1199 (1981)